



# Materials Lab

Wishawin Lertnawapan

## Abstract

The objectives of the experiment were to use experimental data to determine suitable materials for the manufacture of a pin and rod assembly in an aircraft assembly under a known load, and to analytically calculate a minimum dimension for each respectively through evaluation of material properties. A strut assembly is vital in various areas on the aircraft as the components must be engineered to withstand various modes of loading and unloading at a sufficient level of performance throughout an aircraft's service life.

In the given investigation, three individual tests were performed on a selection of materials namely samples of aluminum, low-carbon steel, cast-iron steel and high-carbon steel: tensile, torsional and the Charpy Impact tests respectively enabling various material properties to be derived from their results. From these tests it was concluded from the available materials, high-carbon steel was most appropriate for the rod with a minimum diameter of 19.2mm, with aluminum considered as the suitable metal for the pin and a corresponding diameter of 9.12mm.

## 1. Introduction

By assessing and evaluating between various materials and their modes of failure through experimentally standardized procedures, appropriate materials can be utilized for different purposes. Each material exhibits different behaviors under each separate mode of loading; thus computing and selective analysis between these values is vital for investigating them and the method of loading in which each is strongest.

Various industrial applications employ these values in practice - an aircraft strut/bracket assembly is used in the given situation, consisting of a connection between a rod and a pin module as shown in Figure 1.1., utilized in various areas along an aircraft's infrastructure. These include integration into the fuselage substructure, cargo struts, wingbox support and fastening of cabin components - the variety of applications and fundamentals demonstrate the importance of engineering an appropriately strong component to withstand the required loads. This significance is intensified by the increasing demand of commercial airline industries and growing number of aircraft in service.

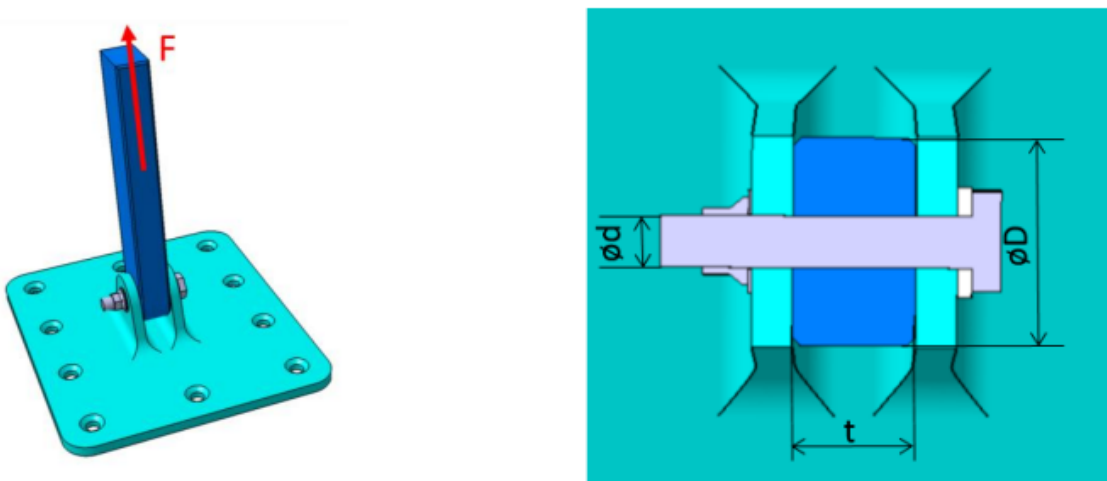


Figure 1.1 a,b - Rod and Pin assembly model [1]

In most circumstances, known parameters impose constraints which must be considered; in general, the structure must withstand a known load, and is restricted to maximum dimensions. For the given scenario, the rod is limited by both the applied force  $F$  acting is purely tensile with a magnitude of  $5 \times 10^4 \text{ N}$ , and its thickness  $t = 0.01 \text{ m}$ . The objective in the lab is to ensure both the rod and pin materials and unconstrained dimensions were selected accordingly to ensure no plastic deformation or fracture would occur as a result of the load, and would remain at an acceptable level of performance under various temperatures experienced between flight and landing can range between extremes of  $-54^\circ\text{C} \sim 60^\circ\text{C}$  and up to  $+1425^\circ\text{C}$  [2] within the combustor sections. The following lab supposes the rod is experiencing pure tensile load, with the pin component conversely under pure shear loads.

To maintain a suitable margin of error, an engineering safety factor of  $S_f = 1.3$  was applied (elaborated in the discussion section); this is to ensure tolerance from poorly manufactured parts or pre-existing internal fractures which can amplify from repeated subjection to loading fatigue into potentially extensive damage.

## 2. Method

The procedure of the experiment was carried out across three different equipments to allow different types of material evaluation and selection between uniaxial, energy and shear analyses respectively. Every sample was individually measured:

A micrometer was used to quantify the diameters for all samples used for the calculation of cross sectional areas and standardization - these measurements were taken along 3 instances across the length of the gauge before being averaged for reliability.

For the tensile and torsion tests, longer gauges were required which exceeded the range of a micrometer, thus accurate readings were taken by using a vernier caliper.

### 2.1. Tensile Test

The tensile test procedure involved the use of an Instron machine (refer to Figure 2.1) to deliver constant uniaxial tensile stress to a sample - the strain of which is observed digitally by the integrated software to produce a stress/strain curve allowing analysis of the different material specimen. Larger samples were required as mechanical properties vary significantly at very small sizes due to small material imperfections thus gauges with diameters of ~10mm and a length of ~50mm were used; the materials tested in this section of the experiment were samples of high-carbon steel, low-carbon steel and aluminum.

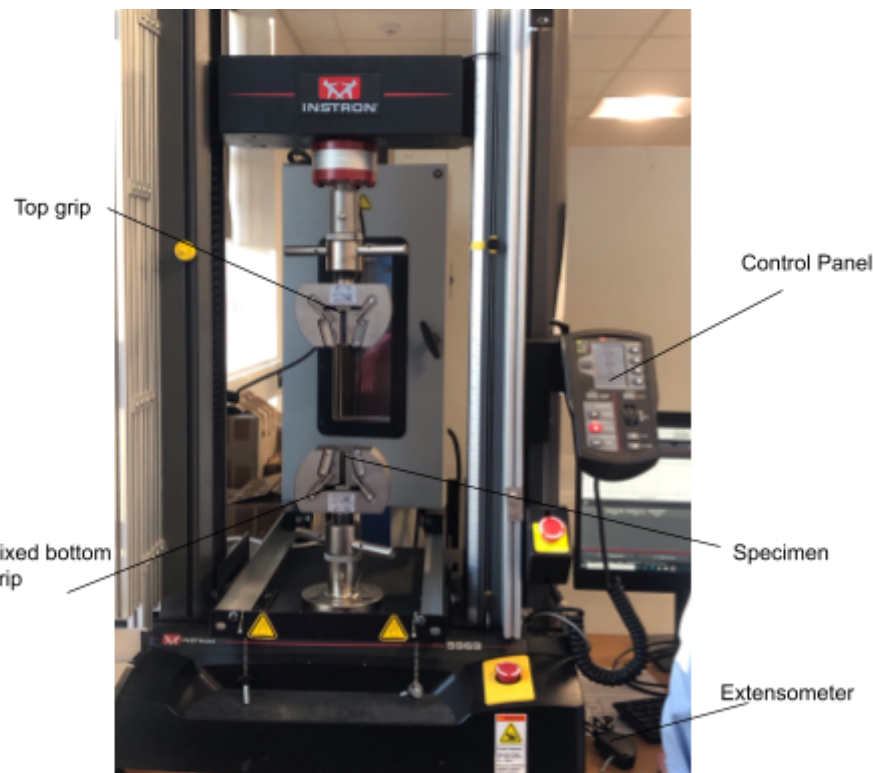


Figure 2.1 - Labeled diagram of the tensile testing equipment

The sample, after dimensional measurements - is placed upright into the bottom grip and tightly secured while the top grip is lowered to clamp on the complementary end to ensure the gauge is configured properly. A sensitive extensometer was attached to the midpoint of

**MENG10005 – Lab Template**

The gauge to measure change in length, where is the dependent variable plotted as the strain against the load over area, stress.

Before data was collected, an initial stress of 0.5kN was applied between the clamps to ensure the specimen is appropriately gripped (preloading). After this load is zeroed, the machine is allowed to apply the tension linearly until the sample deforms; in the results it is shown that the material undergoes several phases of deformation before eventually visibly necking and ultimately failing.

## 2.2. Charpy Impact Test

Measurement of impact energy absorbed by a material sample at different temperatures was done through the Charpy Impact test; utilizing the potential energy loss of a pendulum as it impacts a small standard sample (~3mm in diameter) with a notch by observing the subsequent height of the pendulum after impact. The difference in angle directly correlates to the magnitude of energy loss being absorbed and dissipated into other forms due to the impact with the specimen. Initially a cut was made into each of the 6 cylindrical samples to the same depth (half the cylinders' depth) by using a hacksaw with a cutting block, with the specimen fastened securely in place by a table clamp. The samples used were high-carbon steel, low-carbon steel, and aluminium. 2 samples of each material were identical; one of each was placed into a canister of dry ice and isopropyl alcohol for 5 minutes to lower the temperature to -78°C, measured using a thermocouple.

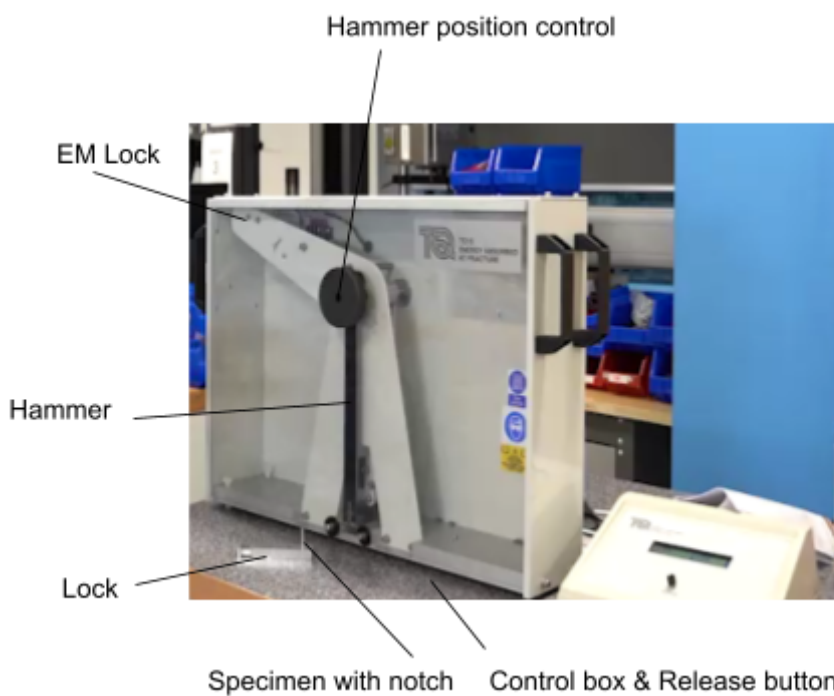


Figure 2.2 - Labeled diagram of the Charpy Impact machine

For samples, each was slotted securely into the shearing block, with the notch facing the direction of the hammer impact. Before the sample is inserted into the Charpy Impact

**MENG10005 – Lab Template**

In addition (Figure 2.1), the hammer was ensured to be reset at the top position - attached to the electromagnetic lock using the external digital hammer control. Once inserted, the lock was detached with the hammer released via the control box; swinging in a pendulum motion before impacting and breaking the sample. Note that for repetitions involving specimens in acetone and dry ice, this process was done quickly to ensure limited temperature change of the sample which may affect the results negatively.

### 2.3. Torsion Test

To demonstrate a material's shear properties for evaluation, a torsion test machine (Figure 2.3) was used to apply a constant rotational force - referred to as torque relative between two ends of the gauge about the longitudinal axis while the rotational angle was measured through the torque meter. Torque was slowly increased linearly in similar fashion to the tensile test until the material reached failure, this enabled the calculation of a material's torsional strength, toughness, and ductility.

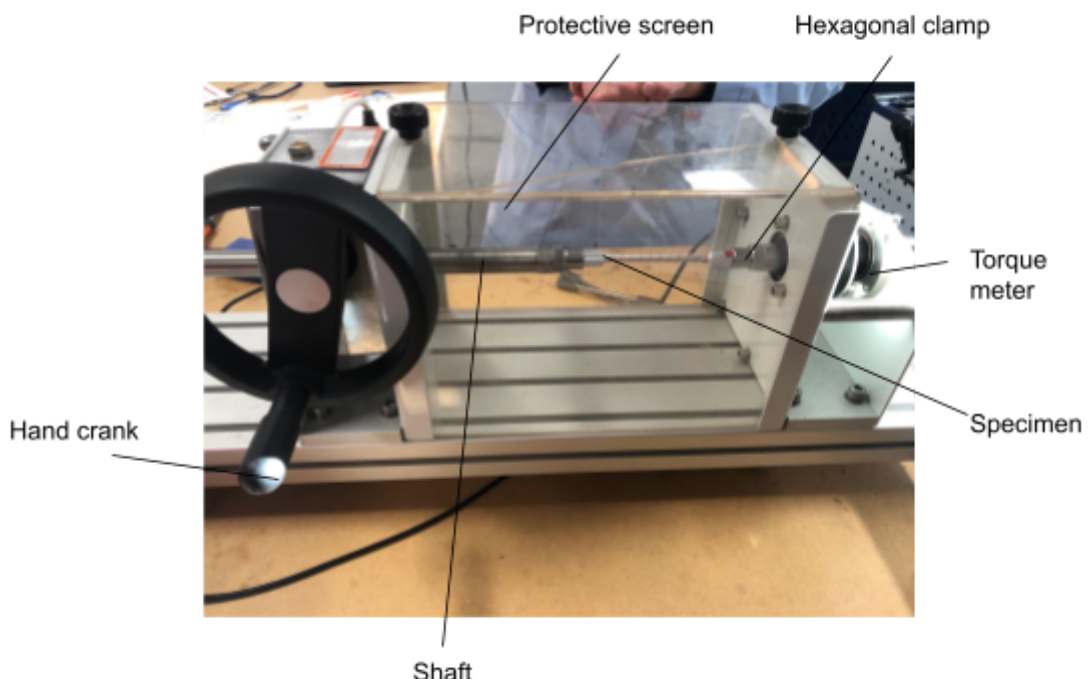


Figure 2.3 - Labeled diagram of the torsional testing equipment

Samples in this test have hexagonal-shaped cross sections at either end to complement tightly to the shape of the clamp sockets, with a thinner circular gauge; on which a line was drawn along the neutral axis to visibly show torsional effects. Different materials were used in this experiment, namely high-carbon steel was replaced with that of cast iron while aluminum and low-carbon steel were kept constant. Once dimensional readings were taken, the specimen was attached to the shaft and clamped tightly and the glass protection was lowered. Then the hand crank was rotated manually at a constant speed; initially, a small torque was added ( $<0.1\text{Nm}$ ) and the gauge zeroed to ensure the test sample was secured. At specific intervals of rotational angles (measured on the control panel), the torque was read off of the second control panel display until the material reached failure ie. the torque meter returned to zero.

### 3.1. Tensile Test Results

Table 3.1 - Tensile Specimen Dimensions

Specimen	Diameter /mm				Gauge Length /mm
	1	2	3	Average	
High-C Steel	9.93	9.93	9.92	9.93	49.15
Low-C Steel	9.92	9.93	9.93	9.93	49.15
Aluminum	9.93	9.94	9.93	9.93	47.80



Figure 3.1 - Gauge samples after tensile testing (from top to bottom: High-carbon steel, Low-carbon steel, Aluminum); note the necking

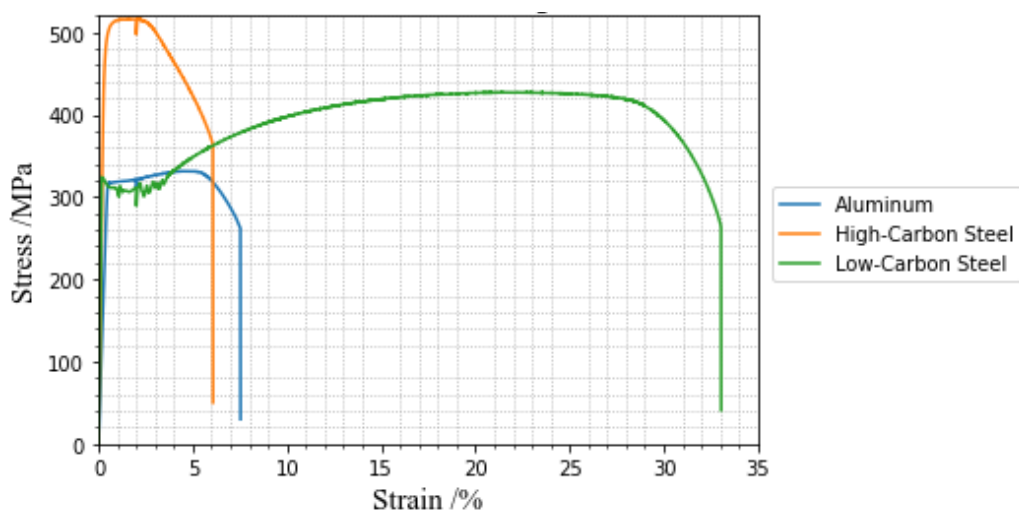


Figure 3.2 - Plot of each specimen under tension using Stress/Strain

## MENG10005 – Lab Template

Figure 3.2 plots the relationships between engineering stress (calculated from dividing instantaneous force applied by cross sectional area given above) and strain. From the graph, multiple material properties can be concluded from analysis of results.

In particular, graph analysis can be predominantly analyzed in two sections. Observations of Figure 3.3 show the general stress-strain graph pattern of a metallic material; of which the “true” curve is superimposed on the “engineering” curve. This distinction is only apparent at the ultimate tensile stress, where the onset of necking in a material causes divergence as the instantaneous area decreases over time as opposed to the engineering curve which assumes a constant cross sectional area [3].

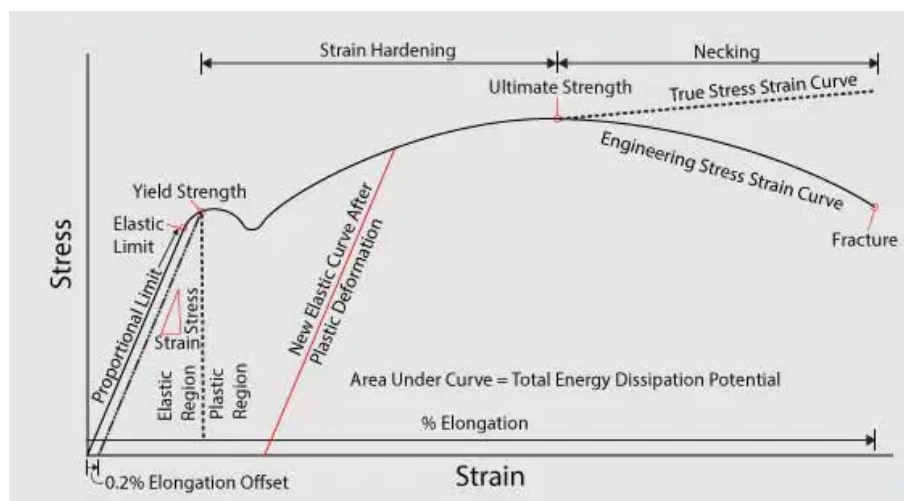


Figure 3.3 - Stress-strain curve of a metal specimen [4]

True experimental values -  $\varepsilon_T$  and  $\sigma_T$  - from the tensile test were converted into engineering data;  $\varepsilon$  and  $\sigma$  for analysis using equations 1 and 2.

$$\varepsilon_T = \ln\left(\frac{L}{L_0}\right) \ln(1 + \varepsilon)$$

$$\therefore \varepsilon = e^{\varepsilon_T} - 1 \quad (1)$$

Where  $L_0$  is the initial gauge length assumed to be unchanged in the engineering curve. Additionally,

$$\sigma_T = \frac{P}{A_i} = \sigma(1 + \varepsilon)$$

$$\therefore \sigma = \frac{P}{A_0} = \frac{\sigma_T}{(1+\varepsilon)} \quad (2)$$

Note the true stress inversely related to  $A_i$  - the instantaneous cross sectional area at the given stress/strain, conversely  $A_0$  used in calculating engineering stress remains constant. Limiting the strain range to 0 - 0.7% reveals a clear distinction between the linear elastic region and its transition into the plastic region, shown in Figure 3.4;

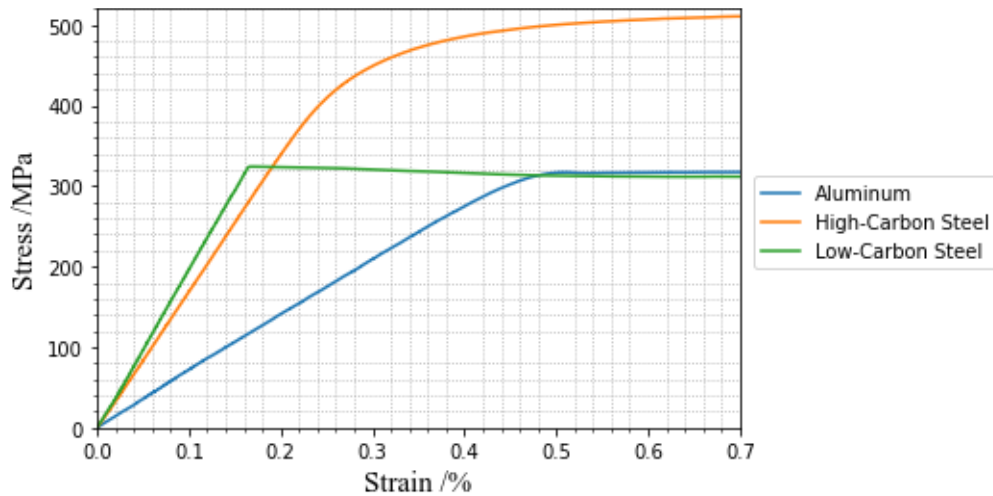


Figure 3.4 - Plot of values between the strain ranges 0 - 0.7%

From these ranges within the elastic region, the Young's Modulus ( $E$ ) was calculated using linear regression against the data set, as the modulus is in practice the gradient of the stress-strain plot, elicited in equation 3;

$$E = \frac{\Delta\sigma}{\Delta\varepsilon} \quad (3)$$

Within the elastic region, yield strength ( $\sigma_y$ ) is an additional useful material property to be calculated in material selection - defined as the maximum stress a material can be applied before elastic deformation terminates. Yield strength however is difficult to accurately define as most metals yield gradually; as an alternative the proof stress, or offset stress ( $\sigma_{0.002}$ ) is utilized; notated as the point where the material exhibits a strain of  $\varepsilon = 0.002$  or 0.2%. By finding the intersection of the tensile curve with a line parallel to the elastic region offset by the strain plotted in Figure 3.5, the proof stress can be determined.

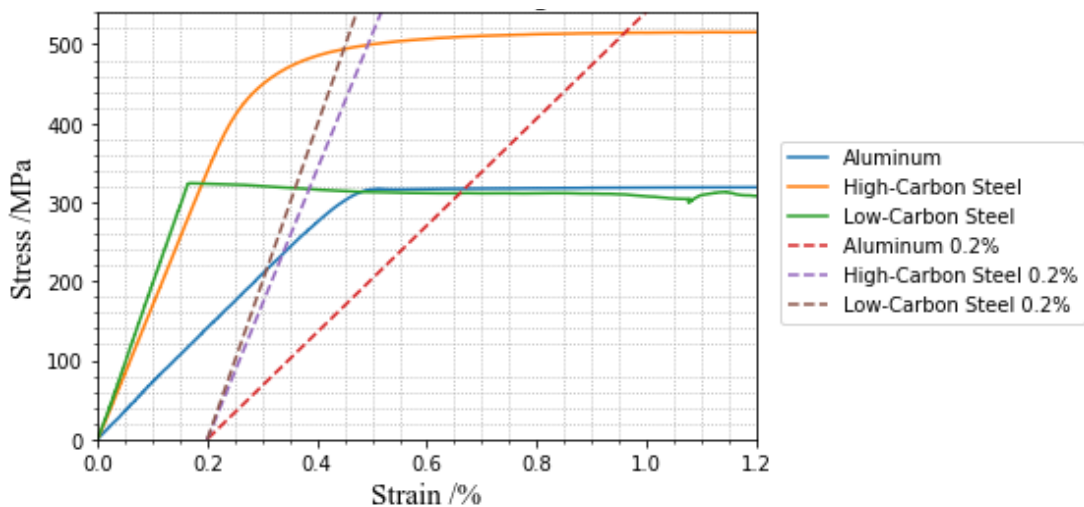


Figure 3.5 - Proof stress calculation plot

An additional intrinsic property beneficial to indexing between suitable materials is the maximum engineering stress at any point prior to fracture - usually occurring immediately at the point where the specimen transitions from strain hardening and exhibits necking; this is referred to as the ultimate tensile strength denoted “ $\sigma_{uts}$ ”.

Likewise on the averse axis, the maximum strain at the point of fracture is labeled as the failure strain, regardless of the phase of deformation which the material is undergoing. In applicatory methods this is often rescripted as average ductility - displayed in equation 4 [5].

$$\varepsilon_{max}\% = \frac{L_f - L_0}{L_0} \times 100 \quad (4)$$

It is important to consider that this measure of ductility is a less accurate indicator of ductility than analyzing the percentage reduction in area, as the deformation across the specimen is not uniform across the gauge length, being highest at the necking point. However, this measure of ductility is a viable comparison measurement as the cross-sectional area of the test piece was not recorded.

Finally, resilience  $R$  and toughness  $W$  are a quantitative analysis of material's ability to absorb tensile energy prior to yielding or failing respectively; determined by integrating the stress-strain plot to derive the graph's area. Materials which are considered tough retain balance between high ductility and high average stress - the modulus of toughness can be computed through integration, providing a more veridical measurement. Toughness is an indicator of total energy absorbed by a specimen; with the majority contributing to plastic deformation. Conversely, the resilience is a measure of energy solely in the elastic domain which also defines the maximum energy which can be released upon unloading, while retaining the atomic lattice - calculated via equation 5 [6]:

$$R = \frac{\sigma_{0.002}^2}{2E} \quad (5)$$

Table 3.2 - Summary of Tensile Test Properties

Specimen	Young's Modulus ( $E$ ) /GPa	Proof Strength ( $\sigma_{0.002}$ ) /MPa	Tensile Strength ( $\sigma_{uts}$ ) /MPa	Average Ductility ( $\varepsilon_{max}$ ) /%	Resilience ( $R$ ) /MJ m <sup>-3</sup>	Tensile Toughness ( $W$ ) /MJ m <sup>-3</sup>
High-C Steel	170.73	338.75	517.18	6.07	0.336	351.79
Low-C Steel	198.64	323.29	427.17	33.04	0.263	1421.22
Aluminum	67.68	141.18	331.58	7.53	0.147	312.69

### 3.2. Charpy Impact Test Results

Table 3.3 - Charpy Impact Specimen Dimensions

Specimen	Diameter /mm				Cross-sectional Area /mm <sup>2</sup>
	1	2	3	Average	
Aluminum, 22°C	3.17	3.17	3.16	3.17	7.89
Aluminum, -78°C	3.12	3.14	3.14	3.14	7.75
High-C Steel, 22°C	3.20	3.21	3.20	3.20	8.04
High-C Steel -78°C	3.21	3.19	3.19	3.20	8.04
Low-C Steel 22°C	3.10	3.09	3.10	3.10	7.55
Low-C Steel -78°C	3.08	3.09	3.09	3.09	7.50

Table 3.4 - Charpy Impact Test Results

Specimen	$\beta$ (Final Angle) / °	PEL (L) / J	Total Fracture
Aluminum, 22°C	85	0.57	Yes
Aluminum, -78°C	86	0.53	Yes
High-C Steel, 22°C	57	1.64	No
High-C Steel, -78°C	58	1.60	No
Low-C Steel, 22°C	88	0.49	No
Low-C Steel -78°C	87	0.44	Yes

Fracture energy is calculated as the quantity of energy absorbed by the sample when impacted by the hammer - this can be interpreted as equivalent to the energy lost between the initial and final position of the hammer.

For all cases, initial angle  $\alpha = 99^\circ$ , whilst  $\beta$  is listed in the results in Table 3.4.

The potential energy of the hammer is a function of its height (equation 6-8);

$$E_p = mgh \quad (6)$$

Where,

$$h_1 = r + r \sin(\alpha - 90^\circ) \quad (7)$$

$$h_2 = r + r \sin(\beta - 90^\circ) \quad (8)$$

Accounting for the small variable energy losses (PEL) between the two positions; the general equation for fracture energy loss simplifies to:

$$G = mgr(\cos\beta - \cos\alpha) - L \quad (9)$$

Where  $m$  is the mass of the hammer,  $g$  is the gravitational constant of acceleration, and  $r$  is the length of the hammer to the center of mass.

It is assumed that  $m = 2\text{kg}$ , and  $r = 0.35\text{m}$

Impact “value” is a standardized numerical value; a function of the impact energy,  $E$  divided by the cross sectional area of the specimen calculated from the measured diameters listed above in table 3.3, leading to the results in table 3.4 below which is a measure of a material’s toughness;

Table 3.4 - Calculated results from Impact testing

Specimen	Fracture Energy ( $G$ ) / J	Impact Value / $\text{Jmm}^{-2}$
Aluminum, 22°C	1.10	0.139
Aluminum, -78°C	1.02	0.132
High-C Steel, 22°C	3.17	0.394
High-C Steel, -78°C	3.11	0.387
Low-C Steel , 22°C	0.99	0.131
Low-C Steel -78°C	0.82	0.109

An alternative method to calculating the index of a material’s fracture toughness with respect to temperature is through derivation of the critical stress intensity factor,  $K_c$  [7].

It is assumed that the mode of fracture is mode I (opening)[8], as the stress acts perpendicularly to the crack plane, thus  $K_I$  is used accordingly [9].

Using the general formula for fracture energy  $G$  (equation 10);

$$G = Y \frac{\sigma^2 a \pi}{E} \quad (10)$$

Where  $Y$  is the geometric factor = 1,  $\sigma$  the applied stress, and  $a$  the crack length - assumed to be half the gauge lateral section. Rearranging equation 10 -

$$\sqrt{EG} = \sigma\sqrt{a\pi} \quad (11)$$

Using the minimum threshold stress intensity factor when  $K_1 = K_c$ , the fracture toughness is expressed in equation 12 as;

$$K_c = \sqrt{EG} \quad (12)$$

Thus, the index for fracture toughness for each specimen is reviewed in table 3.5

Table 3.5 - Fracture toughness of specimen

Specimen	Fracture Toughness ( $K_c$ ) / MNm <sup>-3/2</sup>	$\Delta$ Fracture Toughness ( $\Delta K_c$ ) / MNm <sup>-3/2</sup>
Aluminum, 22°C	43.36	1.63
Aluminum, -78°C	41.73	
High-C Steel, 22°C	79.35	0.75
High-C Steel, -78°C	78.60	
Low-C Steel , 22°C	25.89	2.33
Low-C Steel -78°C	23.56	

### 3.3. Torsion Test Results

Table 3.6 - Torsion Test Specimen Dimensions

Specimen	Diameter /mm				Gauge Length /mm
	1	2	3	Average	
Cast Iron	5.93	5.94	5.93	5.93	76.7
Low-C Steel	5.94	5.94	5.93	5.94	75.85
Aluminum	5.93	5.95	5.95	5.94	76.8

Table 3.7 - Torsion Test Results

Cast Iron		Low-Carbon Steel		Aluminum	
Angle $\theta$ /°	Torque $t$ /Nm	Angle $\theta$ /°	Torque $t$ /Nm	Angle $\theta$ /°	Torque $t$ /Nm
0	0	0	0	0	0
10	3.22	10	2.50	20	6.51
20	9.44	20	16.70	40	7.27
30	11.56	30	20.52	60	7.56
40	12.57	40	21.37	80	7.80
50	13.25	50	21.58	100	7.97
59.03	13.64 Failure	100	21.33	200	8.74
		150	21.20	400	9.70
		200	21.11	600	10.23
		300	21.00	800	10.58
		400	20.99	1000	10.72
		500	20.96	1250	10.86
		750	20.95	1500	10.93
		1000	20.97	1750	11.01
		1200	20.91	2000	11.07
		1217.23	13.71 Failure	2250	11.16
				2500	11.26
				2750	11.35
				3000	11.47
				3216.85	11.60 Failure



Figure 3.6 - Gauge samples after torsion testing (from left to right: High-carbon steel, Cast-iron, Aluminum); note the spiral longitudinal lines about the gauge as the indicator

To quantify a material's tendency to deform under rotational or shear stress elastically, the shear modulus of each material is calculated by using several equations. Firstly, measured values of rotational angle were converted into shear strain through equation 13, while torque concurrently was related to shear stress using equation 14 and data from table 3.6;

$$\gamma = \frac{r\theta}{L} \quad (13)$$

$$\tau = \frac{rt}{J} \quad (14)$$

Where  $r$  and  $L$  are constants regarding the radius and gauge length of the specimen respectively.

$J$  is the polar moment of inertia - an index of a shaft's resistance to deformation by torsion as function solely by its cross sectional geometry; expressed in equation 15 and table 3.8:

$$J = \frac{\pi r^4}{2} \quad (15)$$

Table 3.8 - Summary of specimen polar moment of inertia

Specimen	$J / \times 10^{-10} \text{ m}^4$
Cast-iron	1.214
Low-carbon steel	1.222
Aluminum	1.222

Plotting the graph in Figure 3.7;

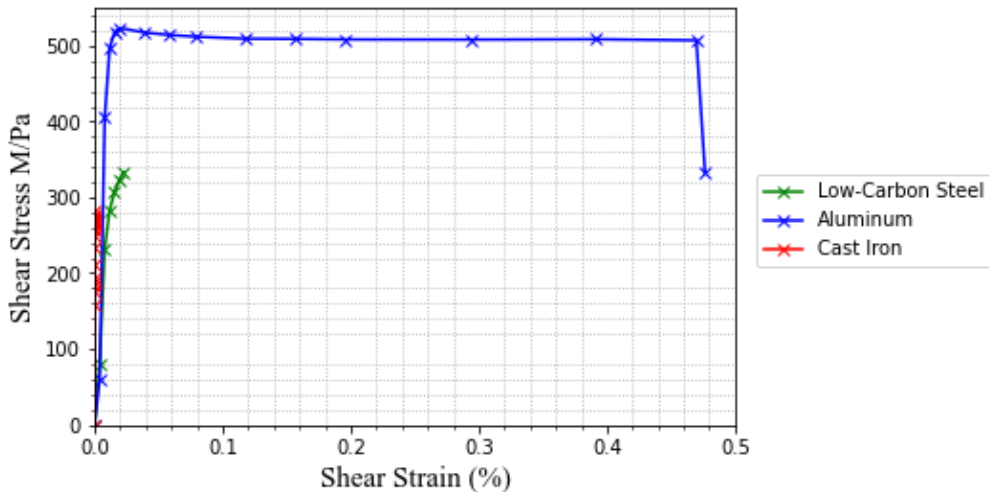


Figure 3.7 - Plot of each specimen under tension using Stress/Strain

By the relationship of equation 16, the expression to rudimentarily derive the value of the shear modulus from the graph is in similar fashion to the Young's Modulus in the tensile portion of the experimental analysis; ie. the gradient of the linear elastic zone - shown more explicitly in strain ranges between 0 - 0.015% in Figure 3.8. Due to the nature of the experimental procedure and the behavior of torsional loading, this linear section is less obvious than the tensile counterpart.

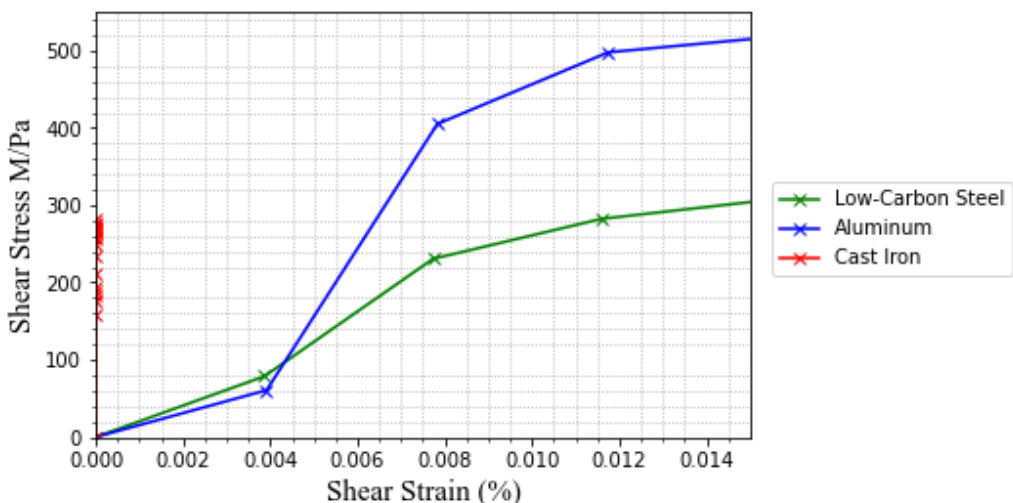


Figure 3.8 - Plot of values between shear strain ranges 0 - 0.015%

$$G = \frac{\Delta\tau}{\Delta\gamma} \quad (16)$$

Substituting equations 13 and 14 and factoring constant terms  $r$  and  $L$ , the expression for shear modulus can be shown as a function of  $t$  and  $\theta$ ;

$$G = \frac{tL}{J\theta} \quad (17)$$

Torsional toughness is acquired directly as a product between the shear strain and the shear stress; as performed identically to the tensile section of the experiment, this was accomplished by computing the integral of the data in Figure 3.7 and likewise is quantitatively a measure of the maximum energy absorbed by a specimen prior to failure. The distinction between tensile toughness,  $W$  and torsional toughness  $W_t$  is important to consider, as different methods of loading significantly alter the performances and consequently the relative toughness values between each material. When considering aluminum as an example, this discrepancy is evident; shown between tables 3.2 and 3.9: the material rated the highest with energy absorbed when the load was exerted rotationally however ranked lowest when the force was applied axially.

Proof shear stress was attempted using the 0.002 strain offset parallel, however due to difficulties in determining the intersection between the line and the plotted data points (Figure 3.9); this method was rejected, instead the maximum acceptable shear stress value within the linear division was considered and proceeded as the yield stress,  $\sigma_y$ .

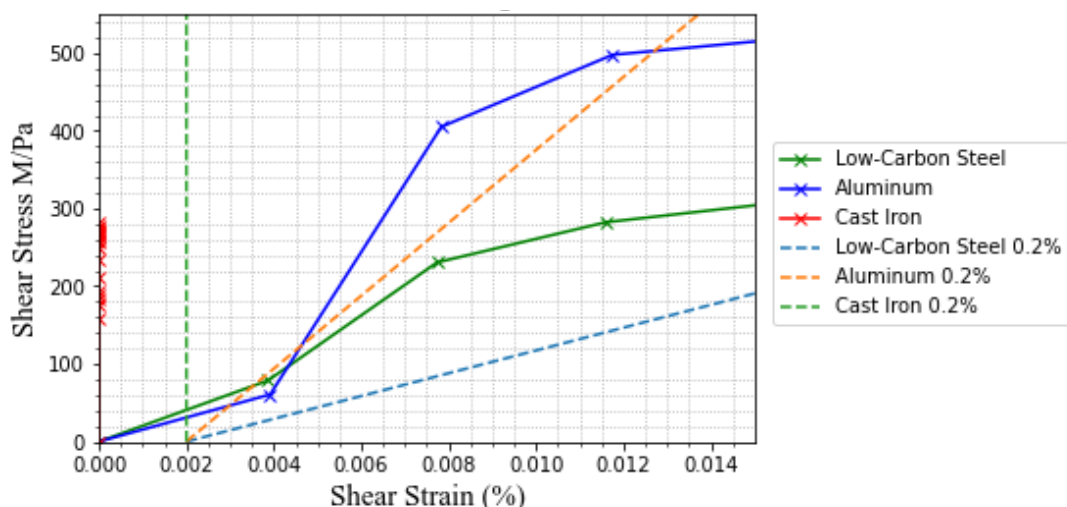


Figure 3.9 - Unsuccessful proof stress calculation plot

Table 3.9 - Torsional test materials summary

Material	Shear Modulus (G) /GPa	Toughness ( $W_t$ ) /MJm <sup>-3</sup>	Yield Shear Stress ( $\sigma_y$ ) /MPa
Cast Iron	735.21	138.87	189.22
Low-C Steel	46.94	441.50	307.00
Aluminum	14.67	676.70	497.80

## 4. Discussion

### 4.1. Experimental value evaluation

The following section analyzes the outcomes of each of the procedures and attempts to justify the behaviors of each material by application of the physics governing metallurgy to describe the general trends.

By using and comparing results to existing literature, each of the tests can be validated through both graphical behavior in the graph plots and ultimately the calculated results from tables 3.2, 3.4, 3.5 and 3.9 respectively to evaluate the margin of error. If these are present, elaboration and consideration of potential improvements in the following section are included.

#### 4.1.1. Tensile Test

Using trends observed in Figure 4.1 and comparing with the experimental data, the trends of each material were shown to closely align. In particular, the plastic region of mild steel shows higher value of average ductility than steels with higher percentages of mixture as indicated by the percentage elongation at failure.

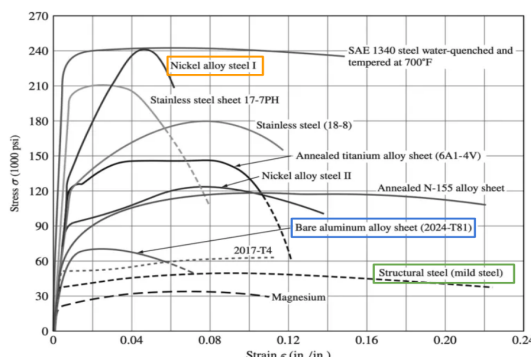


Figure 4.1 - Literature stress-strain graph of different metals [10]

Table 4.1 compares average theoretical and experimental values between the young's modulus, yield (proof) strength and failure strain.

Table 4.1 - Comparison of actual and experimental tensile test results [11,12,13]

Material	Young Modulus ( $E$ ) /GPa		Proof Stress ( $\sigma_{0.002}$ ) /MPa		Failure Strain ( $\varepsilon_{max}$ ) /%	
	Actual	Experiment	Actual	Experiment	Actual	Experiment
High-C	200	170.73	896	338.75	14.3	6.07
Low-C	202	198.64	519	323.29	53.4	33.04
Aluminum	77.4	67.68	278	141.18	9.9	7.53

From the table, results deviate in comparison noticeably; however general trends were respected - ie. The young's modulus of low-carbon is discerned to be highest, followed by high-carbon then aluminum with a significant difference accordingly. This is in correspondence with general trends which generalize for most cases: as the proportion of alloying elements increases, the resulting steel increases in yield and maximum stress, however at the cost of increased brittleness.[14].

#### 4.1.2. Charpy Test

The main objective of the Charpy test was to determine fracture toughness, ie. the quantity of energy absorbed by the standard specimen in the specific mode of fracture. Additionally, the assessment for fracture toughness,  $K_c$  was also calculated; as this index accurately gauges a material's ductility change with respect to temperature. As the nature of the experiment was a tensile load applied to a notch position, the experiment subjects the specimen to fractures propagating throughout - brittle materials will not plastically deform as effectively causing localized stress concentration at the crack tip resulting in larger fracture lengths thus absorbing less energy before failure.

Specimens exhibit loss of ductility when the material temperature is decreased; if the temperature experienced is low enough the specimen may transit through the ductile to brittle temperature (DBTT), this phenomenon occurring due to decreased ability to form dislocation slips at the crack tip to form plastic regions. Without sufficient thermal energy, the process virtually ceases at low enough temperatures causing cracks to propagate quickly and ductile failure to occur [15].

In figure 4.2, the trend implies a steeper gradient between fracture energies between positions of temperature with a higher energy difference; as the carbon percentage of mixture decreases within the steel. The difference in fracture toughness  $\Delta K_c$  was greatest in low-carbon steel (2.33) and smallest in high-carbon steel (0.73) - observations of which are supported by the graph. The large difference corresponds to low-steel ~0.11% carbon directly transitioning through the DBTT between -78 and 22°C; this explicitly is not sustained by steel containing >0.31% carbon (considered as high carbon steel).

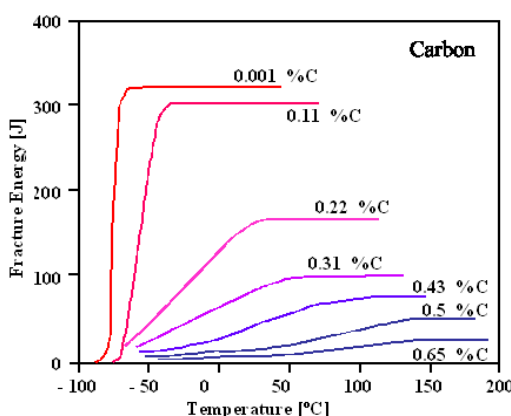


Figure 4.2 - Different fracture energies plotted against temperature on varying carbon percentages [16].

Results of the Charpy test and proceeding calculations are inconsistent with the literature readings in table 4.2 though all specimens show negative correlation between temperature and fracture toughness.

Table 4.2 - Comparison of actual and experimental Charpy test results

Material	Fracture Energy ( $G$ ) /J		Fracture Toughness $K_c$ /MPa m <sup>-3/2</sup>	
	Actual	Experiment	Actual	Experiment
Aluminum, 22°C	7.91	1.10	47.3	43.36
Aluminum, -78°C	-	1.02	-	41.73
High-C Steel, 22°C	34.1	3.17	60.1	79.35
High-C Steel, -78°C	-	3.11	-	78.60
Low-C Steel , 22°C	54.9	0.99	68.2	25.89
Low-C Steel -78°C	-	0.82	-	23.56

The majority of error sources in the Charpy test manifested due to the small specimen sizes. As the test is a low-cost standard, small imperfections in the materials and human sources of uncertainties can lead to significant errors in the final result. These uncertainties include inconsistencies in the notch dimensions which define the elastic stress concentration factor ( $K_t$ ) [17], notch surface defects during sawing, micrometer diameter reading errors, inaccurate sample temperature measurements, or potentially poor calibration of machine and energy loss in the test system [18]. More repeats should be performed to cumulate a suitable number of trials for an average to be determined.

It is also highly likely the measure of high-carbon steel fracture energy and toughness is inaccurate and marginally lower than the actual values due to the specimen in both temperature instances failing to fracture completely, producing an unstandardized test between materials.

#### 4.1.3. Torsion Test

All experimental torsion test results were less accurate than the tensile counterparts; this was majorly due to a substantially smaller data set with a much smaller sample rate in contrast to the tensile computer, but also innately as consequence of a material's elastic region under pure torsion lasting to a smaller degree of strain. From the results in table 3.9, aluminum is observed to perform better than both forms of steel when intrinsic yield shear stress, toughness - and graphically ductility via failure strain are compared.

Torsional toughness data can be verified through the nature of the fracture fault: literature trends state brittle materials tend to have angled fracture surfaces, while more ductile materials have perpendicular fracture surfaces with the position of fracture emitting more heat due to friction. This occurs as a consequence of uneven stress distributions along the surface of the material in torsion experienced by different sections and their respective twist angles - fracture propagates from the surface towards the interior along the torsion axis [19] where failure occurs along the plane where maximum mode of stress is reached first following maximum-shear-stress theory [20]; for brittle materials tensile stress in the plane (45°) reaches a maximum prior to the shear stress acting along the perpendicular

, thus failure occurs accordingly.

The aluminum specimen fracture angle was close to perpendicular, with the fracture point being noticeably hot immediately after failure; these results are in line with the trends stated earlier. Cast iron contrarily experienced failure at lower rotational angles implying a more brittle material; close inspection of figure 3.6 support this conclusion as the fracture line is more angled and uneven.

Table 4.3 - Comparison of actual and experimental torsion test results[21]

Material	Shear Modulus ( $G$ ) /GPa		Yield Shear Stress ( $\sigma_y$ ) /MPa	
	Actual	Experiment	Actual	Experiment
Cast Iron	58.4	735.21	545	189.22
Low-C	79.7	46.94	-	307.00
Aluminum	19.9	14.67	110	497.80

Table 4.3 is a comparison between the experimental torsion data obtained. Inconsistencies were present across both calculated values, with significant errors between true and investigated results. Notably the values of cast-iron were highly inaccurate with a discrepancy of >1345%; this is likely due to misreading of torque values during the torsion procedure due to low sampling frequency and poor attachment of the hexagonal gauge into the clamps leading to false sensor readings in the machine. The latter is highly probable as the nature of the error is innately systematic due to data deviating by a proportional factor.

Less major deviations from true values of shear modulus in aluminum and low-carbon samples can likely be attributed to inconsistent application of torque through the hand wheel.

Across all tests, certain factors are present which can not be controlled leading to small discrepancies and deviations from the theoretical values. Samples may contain trace levels of impurities which can disrupt physical properties of metals by altering the lattice and redistributing the metal ions, and in alloys can affect the magnitude of this effect based on the percentage of the nonmetal [22]. Small fluctuations in the environmental condition such as the specimen being exposed to inconsistent temperature and humidities may minutely impact the results. Additional factors include microfractures due to manufacturing processes; defects from imperfections in grain boundaries led to slight deviations in yield, ultimate and failure stress numbers during load testing.

#### 4.2. Pin

The pin is a component placed under purely shear stress - more specifically double shear as the load acting transversely against the element is distributed along two planes. First, using the safety factor formula for  $S_f$  in equation 19 [23], a suitable pin diameter  $d$  was determined with the presumption of the common aeronautical standard of 1.3 being

applied.

$$S_f = \frac{\tau_y}{\tau_{max}} \quad (18)$$

$$\tau_{max} = \frac{F}{2\pi r^2} \quad (19)$$

Where  $\tau_y$  is the experimental yield shear stress obtained from table 3.9 - constrained as the maximum allowed shear stress as the component must not deform plastically.  $\tau_{max}$  specifies the magnitude of shear stress the pin is assumed to withstand in practical situations, given by equation 19 above using the double shear stress formula [24] with variable  $\pi r^2$  as the projected cross-sectional area the load  $F$  acts through. The results are shown in the table 4.3 below.

Table 4.3 - Double shear diameter calculations

Material	Minimum Diameter $d$ (mm)
Cast- Iron	14.79
Low-C Steel	11.61
Aluminum	9.12

On the basis of table 3.9, by comparison of shear modulus and yield shear strength values the selection of viable materials for the pin was narrowed to between cast-iron (possessing the highest shear modulus) and aluminum (highest shear yield strength).

Ultimately, aluminum was considered as the most suitable material for the specific component, as a pin manufactured with aluminum would require the least minimum diameter as per table 4.3. Moreover, the behavior exhibited by the torsion graph in figure 3.7 indicates cast-iron as a highly brittle material with a failure strength virtually identical to the yield shear strength. This is undesirable as a ductile fracture is generally considered the preferred mechanism over brittle failure - due to ductile fracture requiring more energy over a gradual increase of stress; which can be perceived as plastic deformation prior to failure to allow the component to be replaced preemptively.

It is worth noting that despite requiring a smaller diameter, it is unlikely the use of aluminum yields economical benefits as the cost index per mass of aluminum is higher than both cast-iron and mild steel.

### 4.3. Rod

The guidelines assumes the load applied along the rod is purely tensile, limiting considerations to evaluate to table 3.2; more unambiguously, the materials' yield/proof stress was considered as the innate property instead of the ultimate tensile stress, as this component must also not deform plastically. Equation 19 was rearranged with proof and maximum tensile strength in place of shear into equation 20. To calculate  $\sigma_{max}$ , the formula

for uniaxial tensile stress was used (equation 21),

$$S_f = \frac{\sigma_{0.2\%}}{\sigma_{max}} \quad (20)$$

$$\sigma_{max} = \frac{F}{A} \quad (21)$$

Where  $A$  - the sectional area normal to the direction of load - can be expressed as  $t(D-d)$  from Figure 1.1b with  $D$  as the unconstrained variable,  $d$  from the minimum acceptable pin diameter of aluminum and  $t = 0.01m$

Table 4.4 - Rod diameter calculations

Material	Minimum Diameter $D$ (mm)
High-Carbon Steel	19.20
Low-Carbon Steel	20.11
Aluminum	46.06

For the rod, high-carbon steel was considered the most appropriate material using tensile yield and Young's modulus properties. As the material tolerates the highest yield strength with a similarly high modulus with a value only ~14% lower than low-carbon steel, the minimum diameter of the rod was calculated to be least in high-carbon steel (Table 4.4) and the resulting rod would be stiffer (ie. smaller strain change during loading).

High-carbon steel rates the highest of the three materials in resilience allowing the highest quantity of energy to be absorbed and released completely while retaining complete elasticity.

With consideration to energy, change in fracture toughness and impact value measured across the two tested temperature points; high-carbon steel performed nominally the highest. Referring to table 3.6, high steel impact values indexed between 3-4 times higher than aluminum and low-carbon steel and was observed to not entirely fracture hence suggesting the material can absorb the highest quantity of energy. This is supplemented by high-carbon exhibiting the lowest change in fracture toughness across the temperature range (communicated in table 3.6); making it viable for the specific application as it retains integrity whilst undergoing temperature fluctuations experienced by aircraft through its stages of operation - reducing potential for brittle fracture to occur under low temperatures.

This, in conjunction with the prices of high-carbon steel (averaging \$2.76/kg less than mild steels and especially aluminum [25]) makes high-carbon steel more economically favored. As plastic deformation is a parameter constraining the assembly, resilience was accounted for in place of toughness as the energy absorbed across loading/unloading should only be limited to elastic deformation.

Despite the higher average ductility present in both aluminum and low-carbon steel, these values are considered with less importance than when applied in the torsion test. When graphs between tension and torsion are comparatively viewed with focus along the strain

## MENG10005 – Lab Template

axis, it is apparent that the proportion of strain percentage experienced by materials undergoing torsion in contrast to tensile is up to two orders of magnitudes smaller. This analysis from a functional and practical standpoint implies the difference between elastic and plastic/failure loading regimes is less visible and thus more precautions should be accounted for when implemented. In consideration to this, the strut/bracket assembly in an aircraft system and referring to Figure 1.1a, it is assumed that the pin component is less visible than the rod - especially in maintenance; therefore it is more important plastic deformation does not occur.

## 5. Conclusion

Through carrying out the standardized tests, and assessment of results it was concluded the most suitable material for the manufacture of the pin and rod are aluminum and high-carbon steel respectively.

Aluminum was the preferred option in the application of shear due to the material's high yield shear strength and toughness. The former allows the minimum diameter of the pin to maintain structural integrity with a diameter of 9.12mm; whilst the high toughness correlates directly to its ductility. In practice this elementary property leads to visible tolerances in plastic deformation allowing such parts to be replaced prior to failure as a precaution.

Using high carbon, a manufactured rod would measure a diameter of 19.2mm with a thickness of 10mm. High carbon was favored over other metals due to a high value of Young's modulus, and marginally largest yield modulus eliciting best economical practicality. The material's highest resilience modulus and low change in integrity across aircraft service temperatures was also recognized as an advantageous property.

Should future experiments be carried out, more reliable values can be obtained through the use of larger specimen gauges to lower random uncertainties caused by material defects and the influence of human error. Finally, the number of trials should be increased for improved reliability across all collected results.

## References

- [1] MENG1005 (2022) University of Bristol: *Engineering by Investigation*, Properties of Materials Lab Instructions, 2  
Retrieved from:  
[https://www.ole.bris.ac.uk/webapps/blackboard/content/listContent.jsp?course\\_id=\\_24652\\_5\\_1&content\\_id=\\_6173386\\_1&mode=reset](https://www.ole.bris.ac.uk/webapps/blackboard/content/listContent.jsp?course_id=_24652_5_1&content_id=_6173386_1&mode=reset)
- [2] Accelerated Aging of Materials and Structures: The Effects of Long-Term Elevated-Temperature Exposure (1996) *Chapter:2 Aircraft Operating Environment*  
Retrieved from:  
<https://nap.nationalacademies.org/read/9251/chapter/4>
- [3] Yasin, C. (2020) Engineering Stress/Strain vs True Stress/Strain  
Retrieved from:  
<https://yasinpar.com/engineering-stress-strain-vs-true-stress-strain/>
- [4] Emmet, C. (2019) The Stress Strain Curve | *Intro To Structural Engineering*  
Retrieved from:  
<https://asreengineering.com/2019/08/14/the-stress-strain-curve-intro-to-structural-engineering/>
- [5] Engineer's Edge *Ductility Review - Strength Mechanics of Materials*  
Retrieved from:  
[https://www.engineersedge.com/material\\_science/ductility.htm](https://www.engineersedge.com/material_science/ductility.htm)
- [6] Retrieved from: <https://mechanicalc.com/reference/mechanical-properties-of-materials>
- [7] Irwin, G. R. (1968) Linear Fracture Mechanics, Fracture Transition, and Fracture Control. *Engineering Fracture Mechanics*, 1, 241-257.  
Retrieved from: <https://matmatch.com/learn/property/fracture-toughness>
- [8] Mecholsky Jr., J. J. (1995) Fracture Mechanics Principles. *Mater.* 11, 111-112.
- [9] Fracture Toughness (n.d.) *UNSW, School of Materials Science and Engineering*.  
Retrieved from:  
<http://www.materials.unsw.edu.au/tutorials/online-tutorials/3-fracture-toughness>
- [10] Sundar (2017) Stress Strain Curve | *Stress Strain diagram*  
Retrieved from:  
<https://extrudesign.com/stress-strain-curve/>
- [11,12,13,21] MatWeb, LLC (1996 - 2022)  
Retrieved from:  
<https://matweb.com/search/DataSheet.aspx?MatGUID=ee25302df4b34404b21ad67f8a83e858&ckck=1>  
<https://matweb.com/search/DataSheet.aspx?MatGUID=034970339dd14349a8297d2c83134649>  
<https://matweb.com/search/DataSheet.aspx?MatGUID=ab8aeb2d293041c4a844e397b5cf>

## MENG10005 – Lab Template

bd4e&ckck=1

<https://matweb.com/search/DataSheet.aspx?MatGUID=6291a24572754cae94ff365ed99b96f9&ckck=1>

[14] Retrieved from:

<https://monroeengineering.com/blog/low-vs-medium-vs-high-carbon-steel/#:~:text=To%20recap%2C%20steel%20is%20often,contains%20more%20than%200.60%25%20carbon>

[15] Adrian, P. M. (2012) Introduction to Aerospace Materials, *Fracture toughness properties of aerospace materials*, 19.3

Retrieved from:

<https://www.sciencedirect.com/topics/engineering/brittle-transition>

[16] Rinebolt , Harris (1951) Transaction Am. Soc. Metals, Vol. 53., 1175

[17] Hiroaki Kurishita et al (1993) Effects of V-Notch Dimensions on Charpy Impact Test Results for Differently Sized Miniature Specimens of Ferritic Steel, *Volume 34 Issue 11*, Retrieved from:

[https://www.jstage.jst.go.jp/article/matertrans1989/34/11/34\\_11\\_1042/\\_article](https://www.jstage.jst.go.jp/article/matertrans1989/34/11/34_11_1042/_article)

[18] M.A., Lont (2000) The Determination of Uncertainties in Charpy Impact Testing, 4-5. Retrieved from:

<https://www.npl.co.uk/getmedia/73d00151-1e60-451e-a666-813861b51225/cop06.pdf/>

[19] Y. Li , et al. (2019) Fatigue properties and cracking mechanisms of a 7075 aluminum alloy under axial and torsional loadings, *Procedia Structural Integrity* 19, 637–644

Retrieved from:

[https://www.researchgate.net/publication/338155475\\_Fatigue\\_properties\\_and\\_cracking\\_mechanisms\\_of\\_a\\_7075\\_aluminum\\_alloy\\_under\\_axial\\_and\\_torsional\\_loadings](https://www.researchgate.net/publication/338155475_Fatigue_properties_and_cracking_mechanisms_of_a_7075_aluminum_alloy_under_axial_and_torsional_loadings)

[20] R.C. Hibbeler | Mechanics of Materials, 525

[22] Joginder, S.G. (2002) Physical Effects of Impurities in Metals, *Chapter 5.1.*, 93.

Retrieved from:

[https://link.springer.com/chapter/10.1007/978-1-4615-1241-7\\_5?noAccess=true](https://link.springer.com/chapter/10.1007/978-1-4615-1241-7_5?noAccess=true)

[23] Engineering ToolBox, (2010). *Factors of Safety*.

Retrieved from:

[https://www.engineeringtoolbox.com/factors-safety-fos-d\\_1624.html](https://www.engineeringtoolbox.com/factors-safety-fos-d_1624.html)

[24] Beer. F.P. , Johnston.E.R. (1992). *Mechanics of Materials* , 2nd edition. McGraw-Hill Retrieved from:

<https://amesweb.info/StressStrainTransformations/Shear-Stress.aspx>

[25] Retrieved from:

<https://agmetalminer.com/mmwp/metal-prices/>